State filtering and nonlinear control of fine tracking system in quantum positioning systems

SHUANG CONG, ZISHENG ZOU, SHIQI DUAN
University of Science and Technology of China
Department of Automation
Jinzhai Road 96, 230027 Hefei
CHINA
scong@ustc.edu.cn

DING CHEN
Beijing Institute of Satellite
Information Engineering
State Key Laboratory of Space-Ground
Integrated Information Technology, 100086, Beijing
CHINA

Abstract: The accuracy of the fine tracking system is the premise of high-accuracy positioning in quantum positioning systems. In this paper, we propose a method combining model reference adaptive control (MRAC) strategy and adaptive strong tracking Kalman filter (ASTKF) to reduce the impacts of satellite platform jitter and environment noise. A mathematical model of the fine tracking system with disturbance and environmental noise are set up and analyzed. Aiming at colored irregular noise signal, we design an ASTKF to estimate the state of the system on-line, at the same time, the disturbance and noise changing with time are also estimated and eliminated. By combining a MRAC strategy, we enhance the robustness of the fine tracking system. Numerical experiments of tracking performances comparing different methods available in the literature are given. The numerical simulation results show that the proposed method can improve the tracking accuracy, and almost 99.7 % of the spots can be projected into the square area within 2 μrad.

Key–Words: quantum positioning, fine tracking control, adaptive filtering, nonlinear control

1 Introduction

The quantum positioning system (QPS) which is based on quantum mechanics and informology has become a promising trend of the future positioning and navigation systems. It can overcome the precision limitation due to classic noise in electromagnetic based positioning systems [1]. By transmitting and receiving the entangled photon pairs and measuring their second order coherence bewteen the quantum satellite and ground user, the QPS can achieve a measurement precision of the time difference of arrival (TDOA) value at femtosecond level, which corresponds to a micron level distance measurement precision. During the working process of the QPS, It needs to set up a bidirectional optical communication link between the quantum satellite and ground user, and transmit and receive the entangled photon pairs through the optical link. This process depends on the acquisition, tracking and pointing (ATP) of position system. The positioning accuracy is strongly related to the performance of the ATP system. Recently, the ATP technique has made a great use in the satellite-ground quantum optical communication. The successful implementations of the three quantum experiments about satellite-to-ground quantum key distribution [2], quantum teleportation [3], entanglement based quantum key distribution [4] on the Micius satellite, Quantum Experiments at Space Scale (QUESS) launched in China in August 2016, have fully verified the feasibility of adopting the ATP system for satellite-ground quantum optical alignment. Due to the characteristics of small beam divergence angles, long transmission distances, atmospheric interference, and satellite vibration, the stability of optical alignment is seriously affected [5, 6, 7]. Therefore, ATP system uses a compound technology of nested fine tracking system in the coarse tracking system to achieve the accurate tracking of quantum photons [8], where the coarse tracking system is mainly responsible for scanning and capturing a large range of beacon light in the initial period and guiding the beacon light spot into the fine tracking field, while the fine tracking system is mainly responsible for accurate tracking and locking of the beacon light and quantum photons. Because the tracking accu-

racy of the ATP compound system depends on the tracking accuracy of the fine tracking system, the fine tracking system is becoming a hot spot of research. Some methods based on the wavelength selection and advanced devices techniques were proposed [9, 10] in fine tracking system. Some advanced controllers were proposed for the precision position tracking, such as the constrained observer-based controller for uncertain stochastic nonlinear discrete time systems with input constraints [11], active disturbance rejection controller [12], embedded self-learning fuzzy controller [13] and sliding mode for positioning and tracking tasks [14], and a novel switching controller incorporated with backlash and friction compensations is utilized to achieve speed synchronization among multi-motor and load position tracking in the paper [15]. Some filters were also studied, such as the recursive-least-squares adaptive filter [16] and the extended Kalman filter [17]. Those methods did improve the tracking accuracy. However, in the existing published papers, there are a few researches on the consideration of the effects of state disturbances and environmental noise in position track systems and the high performance of adaptive reference model controller with filter.

In this paper, we propose a MRAC system with an ASTKF. Because the satellite platform disturbance is time-varying, the ASTKF is designed to on-line estimate the system state and the satellite platform disturbance at the same time to reduce the environmental noise and achieve high accuracy in fine tracking system. Up to now there has not been reported that these advance stratagies had been applied in the quantum positioning systems. In our work, the MRAC system is used to achieve the high performance of less than 2 μrad tracking error in average and the high robustness of the fine tracking system. It is better than the performance of ATP system in QUESS which has an accuracy of 3.5 μrad in average. We establish the fine tracking system model with the influence of disturbance and noise first. Then the internal and external disturbance and environmental noise are analyzed, and the vibration signal of the satellite platform is simulated. The discrete block diagram of the fine tracking system with state disturbance and measurement noise is established. Last, the MRAC with the ASTKF is designed. Numerical experiments of proposed method compared with traditional proportional-integral-derivative (PID) and the auto disturbances rejection control (ADRC) are implemented. The experimental results are analyzed.

The rest of the paper is organized as follows. In Section 2, the model of fine tracking system with state disturbance and environmental noise are established. The method combining MRAC with ASTKF is proposed in Section 3. Numerical experiments are given in Section 4 and the conclusion is in Section 5.

2 Modeling of fine tracking system with disturbance and noise

The structure of the fine tracking system is shown in Fig. 1, which is composed of three parts: 1) a FSM with two axes, 2) an angle deviation acquisition module with a complementary metal-oxide-semiconductor transistor (CMOS) photodetector, 3) a fine tracking controller. The input signal of the fine tracking system is the tracking error of the coarse tracking system, so the fine tracking system can compensate the tracking error in coarse tracking stage and get an ultra-high tracking precision.

The FSM is an actuator composed of a (x-y)-axis frame structure and is used to adjust the angle of incident light. The CMOS sensor receives the incident light reflected by the FSM and converts the light spot on its surface into analogue spot energy current $E(t)$, which is converted into digital spot energy signal $E(k)$ after A/D sampling. After obtaining the digital spot energy signal, the two-axis digital fine tracking angle error $\Delta\theta_F^x(k)$ and $\Delta\theta_F^y(k)$ can be calculated by the angle deviation calculation unit. Then controller generates two digital control signals $u_x(k)$ and $u_y(k)$ according to the designed control strategy. After that, through the D/A converter, $u_x(k)$ and $u_y(k)$ are converted into analogue signals $u_x(t)$ and $u_y(t)$ which drive x-axis and y-axis of the FSM, respectively, and deflect the FSM from an angle opposite to the input coarse tracking angle error, so that the angle deviation between the output angle and the input coarse tracking angle error can be reduced. Because the characteristics of the x-axis and y-axis are similar, we only take one axis as an example. The discrete block diagram of the fine tracking system on the consideration of the satellite platform vibration signal d_θ and the environmental noise v_θ is shown in Fig. 2, in which, $\Delta\theta_C(k)$, the coarse tracking error, is the input signal in the fine tracking control system, $\theta_F(k)$ is the digital deflection angle of the FSM, $\theta'_F(k)$, the FSM deflection angle with measuring noise, is the out-

put signal in the fine tracking system, $S(z)$ is the discrete transfer function of the angle deviation acquisition module, $G(z)$ is the discrete transfer function of the controlled object FSM, which is calculated by Eq. (2). $C(z)$ is the discrete transfer function of the controller that we need to design.

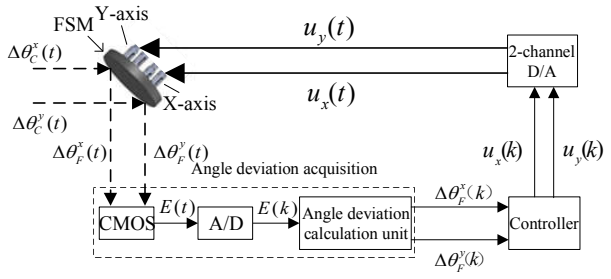

Figure 1: Structure diagram of fine tracking system.

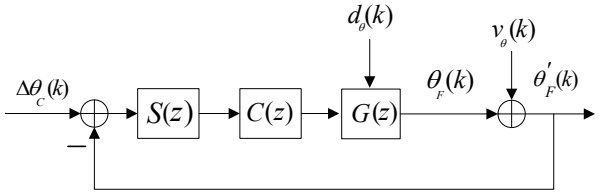

Figure 2: Block diagram of fine tracking system.

In Fig.1, we do the analysis for the x-axis. u_x drives the FSM to deflect an angle θ_F^x along the x-axis direction, FSM's continuous transfer function $G(s)$ can often be considered as a second-order system. So $G(s)$ can be represented by

$$G(s) = \frac{\theta_F^x(s)}{u_x(s)} = \frac{\omega^2}{s^2 + 2\eta\omega s + \omega^2} \tag{1}$$

where ω is the resonant frequency of the FSM, η is the damping coefficient of the FSM. By using the zeroth order retainer to discretize the continuous transfer function of the FSM, its discrete transfer function $G(z)$ can be written as

$$G(z) = \frac{(b_0 + b_1 z^{-1})z^{-1}}{1 + a_1 z^{-1} + a_2 z^{-2}} \tag{2}$$

where

$$\begin{aligned} a_1 &= -2e^{-\eta\omega T}\cos\sqrt{1-\eta^2}\omega T \\ a_2 &= e^{-2\eta\omega T} \\ b_0 &= \left[1 - 2e^{-\eta\omega T}\cos(\sqrt{1-\eta^2}\omega T) + e^{-2\eta\omega T}\right]/2 \\ b_1 &= \left[1 - 2e^{-\eta\omega T}\cos(\sqrt{1-\eta^2}\omega T) + e^{-2\eta\omega T}\right]/2 \end{aligned} \tag{3}$$

and T is the sampling period.

In Fig. 1, the CMOS sensor and A/D sampling convert the analogue fine tracking error $\Delta\theta_F(t)$ into the spot energy signal $E(k)$, and the digital angle deviation calculation unit calculates the digital form signal $\Delta\theta_F(k)$ of fine tracking error through two calculation steps: the acquisition of spot centroid and acquisition of angle (The derivation process of the acquisition of spot centroid and acquisition of angle is in Appendix 1). When the acquisition accuracy of the CMOS sensor is sufficiently high, the angular deviation acquisition module is often approximated as a model with a magnification of 1, and the discrete transfer function $S(z)$ is often expressed as $S(z) = 1$.

In the fine tracking system, the satellite platform vibration and the environmental noise are the main factors affecting tracking accuracy. So, we need to model the satellite platform vibration d_θ and environmental noise v_θ. Generally, the satellite platform vibration is described as the continuous-angular vibration [18, 19]. It can be simulated by inputting a zero mean unit Gauss white noise (ZMUGWN) to a filter obtained from the power spectrum density (PSD) function adopted by the European Space Agency for the semiconductor-laser inter-satellite link experiment(SILEX) program, the PSD function is expressed as $s(f) = 160/[1 + (f/{f_0}^2)]\ \mu rad^2/\text{Hz}$, where f_0 is equal to 1Hz. Through the PSD function, one filter is designed as $F(z) = 0.496(1+z^{-1})/(1-0.9939z^{-1})$. By converting $F(z)$ into a discrete time domain expression, the satellite platform vibration signal d_θ can be formulated as follows

$$d_\theta(k) = 0.99d_\theta(k-1) + 0.49\,(rand(k) + rand(k-1)) \tag{4}$$

where $rand(k)$ is the ZMUGWN at time k; d_θ in time domain is shown in Fig. 3, and numerical simulation of PSD is shown in Fig. 4 to illustrate the rationality of d_θ when it is compared with SILEX program. From Fig. 4, one can see that d_θ we designed satisfies the

PSD characteristic of the satellite platform vibration on the SILEX satellite platform.

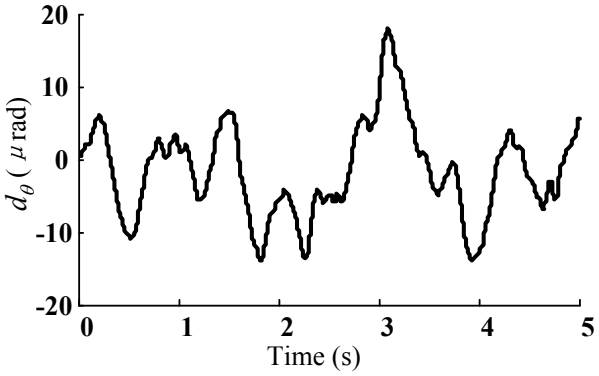

Figure 3: d_θ in time domain.

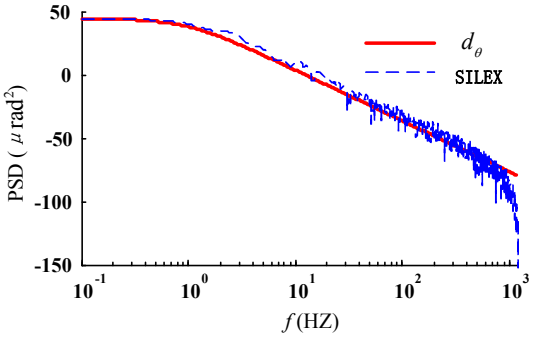

Figure 4: PSD comparison of d_θ and SILEX.

The environmental noise in the fine tracking system mainly includes detector noise, processing circuit noise, spatial background noise and thermal noise. The integrated noise can be regarded as the root mean square of the above noises and is often equivalent to a white noise with an amplitude close to 10 μrad. By carefully debugging the Gauss white noise in MATLAB, we get a model of Gauss white noise with a mean value of 0 and a variance value of 6.5 whose max amplitude is close to 10 μrad. Thus, the environmental noise v_θ is represented by $v_\theta(k) = 6.5rand(k)$, where $rand(k)$ is the ZMUGWN at time k. Then the closed-loop transfer function in fine tracking system with state disturbance and measurement noise is obtained as:

$$\theta'_F(k) = \frac{S(z)C(z)G(z)}{1+S(z)C(z)G(z)}\Delta\theta_C(k) + \frac{1}{1+S(z)C(z)G(z)}v_\theta(k) + \frac{G(z)}{1+S(z)C(z)G(z)}d_\theta(k) \quad (5)$$

The discrete time model of the controlled system $G(z)$ can be written as

$$A(z^{-1})\theta_F(k) = z^{-1}B(z^{-1})u(k) \quad (6)$$

in which, $A(z^{-1}) = 1 - a_1z^{-1} - a_2z^{-2}$,$B(z^{-1}) = b_0 + b_1z^{-1}$, $\theta_F(k)$ is the output of FSM; $u(k)$ is the control input of controlled system.

The discrete time system of the reference model is selected

$$A_m(z^{-1})\theta_F^m(k) = z^{-1}B_m(z^{-1})\Delta\theta_C(k) \quad (7)$$

where, $A_m(z^{-1}) = 1 - \bar{a}_1z^{-1} - \bar{a}_2z^{-2}$; $B_m(z^{-1}) = \bar{b}_0 + \bar{b}_1z^{-1}$, $\theta_F^m(k)$ is the output of the reference model and $\Delta\theta_C(k)$ is the reference input.

3 Design of MRAC and ASTKF

In this section, an adaptive strong tracking Kalman filter (ASTKF) is designed to estimate out the system state and disturbance, and we'll design a model reference adaptive control (MRAC) system to adjust the coefficients of control law and improve the accuracy of the control system. The overall structure of the control system is depicted in Fig. 5, in which the whole control system design is divided into two stages: one the MRAC system design without considering the disturbance and noise, another is ASTKF design with the on-line estimations and eliminations of the disturbance and noise.

3.1 Design of the control law in MRAC system

The design of the control law in MRAC system is given in Theorem 1.

Theorem 1: Consider the controlled system Eq. (6) select the reference model Eq. (7) , the control laws which can make the equation 6 stable are:

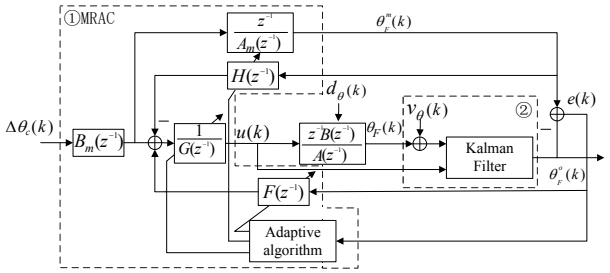

Figure 5: Structure of the control system

$$u(k)=\begin{bmatrix}B_m(z^{-}1)\\H(z^{-1})\\F(z^{-1})\end{bmatrix}^T\begin{bmatrix}\Delta\theta_C(k)\\-\theta_F^m(k)\\-e(k)\end{bmatrix}/G(z^{-1}) \quad (8)$$

where

$$\begin{aligned}H\left(z^{-1}\right)&=h_1\left(k\right)+h_2\left(k\right)z^{-1}\\G\left(z^{-1}\right)&=g_0\left(k\right)+g_1\left(k\right)z^{-1}\\F\left(z^{-1}\right)&=f_1\left(k\right)+f_2\left(k\right)z^{-1}\end{aligned} \quad (9)$$

in which the items in Eq. (9) can be represented as

$$\begin{cases}h_i(k) &= h_i'(k)+\mu_i e(k)\theta_F^m(k-i)\\ h_i'(k) &= h_i'(k-1)+\lambda_i e(k)\theta_F^m(k-i)\\ h_1'(-1) &= 0, h_2'(-1)=0\\ g_{i-1}(k) &= g_{i-1}'(k)+\sigma_{i-1}e(k)u(k-i)\\ g_{i-1}'(k) &= g_{i-1}'(k-1)+\rho_{i-1}e(k)u(k-i)\\ g_0'(-1) &= 15.5, g_1'(-1)=1\\ f_i(k) &= f_i'(k)+q_i e(k)e(k-i)\\ f_i'(k) &= f_i'(k-1)+l_i e(k)e(k-i)\\ f_1'(-1) &= 0.563, f_2'(-1)=0.217\end{cases} \quad (10)$$

where $i=1,2$, and the rest items in Eq. (10) satify

$$\begin{aligned}\lambda_i>0 \quad &;\mu_i\geq-\lambda_i/2\\ \rho_i>0 \quad &;\sigma_i\geq-\rho_i/2\\ l_i>0 \quad &;q_i\geq-l_i/2\end{aligned}$$

The error between the system output and reference model output can be represented as:

$$e(k)=e^o(k)\left[1+\sum_{i=1}^2\begin{bmatrix}l_i+q_i\\ \lambda_i+\mu_i\\ \rho_{i-1}+\sigma_{i-1}\end{bmatrix}^T\begin{bmatrix}e^2(k-i)\\ \theta_F^{m2}(k-i)\\ u^2(k-i)\end{bmatrix}\right] \quad (11)$$

in which $e^o(k)$ is the forecast error:

$$e^o(k)=\sum_{i=1}^2\begin{bmatrix}a_i-f_i'(k-1)\\ a_i-\bar{a}-f_i'(k-1)\\ b_{i-1}-g_{i-1}'(k-1)\end{bmatrix}^T\begin{bmatrix}e(k-i)\\ \theta_F^m(k-i)\\ u(k-i)\end{bmatrix}$$

Next, we will prove the adaptive laws in **Theorem 1** Eqs. (8-11) can stabilize this MRAC system by Popov hyper-stability theory.

Proof: According to the Popov hyper-stability theorem, we will prove that the designed MRAC control laws in Eq. (8) can guarantee the stability of the control system. The proof is divided into three steps: 1) to transform the MRAC system into a standard error feedback control system which consists of two links: the linear link in the forward channel and the nonlinear link in the feedback channel; 2) to prove that the transfer function of the linear link is strictly positive real, and 3) to prove that the nonlinear feedback link satisfies the Popov integral inequality.

We define the generalized output error of the MRAC system as $e(k)=y(k)-y_m(k)$, and by combining error with the Eqs. (6-10) , a system model with the output error $e(k)$ as the controlled variable can be obtained as

$$e(k)=\sum_{i=1}^2\begin{bmatrix}-f_i(k)+a_i\\ -h_i(k)+a_i-\bar{a}_i\\ b_{i-1}-g_{i-1}(k)\end{bmatrix}^T\begin{bmatrix}e(k-i)\\ \theta_F^m(k-i)\\ u(k-i)\end{bmatrix} \quad (12)$$

The structure diagram of system in Eq. (12) is shown in Fig. 6. According to system structure in Fig. 6, let: $v(k)=w_1(k)=e(k)$, and $w(k)=-w_1(k)$, then we have

$$\begin{aligned}w(k)&=-w_1(k)\\ &=-\sum_{i=1}^2\begin{bmatrix}f_i(k)-a_i\\ h_i(k)-a_i+\bar{a}_i\\ g_{i-1}(k)-b_{i-1}\end{bmatrix}^T\begin{bmatrix}e(k-i)\\ \theta_F^m(k-i)\\ u(k-i)\end{bmatrix}\end{aligned}$$

The equivalent feedback control system (11) in Fig. 6 can be equivalently shown as Fig. 7, from which one can see that the transfer function of the linear forward link from w_1k to $v(k)$ is $\frac{v(k)}{w_1(k)}=\frac{e(k)}{e(k)}=1$, which is obviously strictly positive real.

Now we need to prove that the nonlinear feedback link from $v(k)$ to $w(k)$ in Fig. 7 satisfies the Popov integral inequality: $\eta(0,k_1)=\sum_{k=0}^{k_1}w(k)v(k)\geq-r_0^2$,

in which $\forall k_1 > 0, \exists r_0^2 < \infty$. In order to do so, by dividing $r_0^2 = r_f^2 + r_h^2 + r_g^2$, we have:

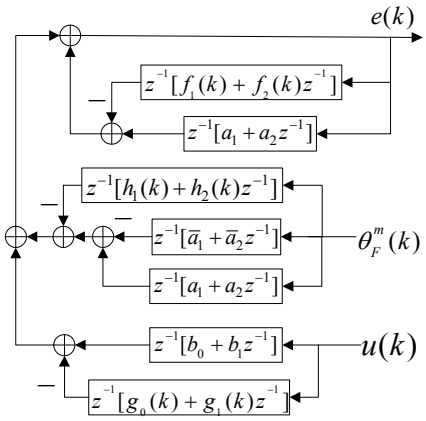

Figure 6: d_θ in time domain.

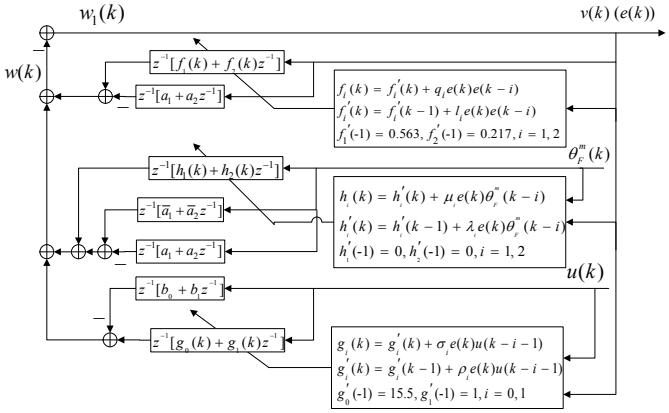

Figure 7: PSD comparison of d_θ and SILEX.

$$
\begin{aligned}
\eta(0,k_1) &= \sum_{k=0}^{k_1} w(k)v(k) \\
&= \sum_{i=1}^{2}\sum_{k=0}^{k_1} \begin{bmatrix} f_i(k)-a_i \\ h_i(k)+\bar{a}_i-a_i \\ g_{i-1}(k)-b_{i-1} \end{bmatrix}^T \begin{bmatrix} e(k-i) \\ \theta_F^m(k-i) \\ u(k-i) \end{bmatrix} e(k) \\
&= \sum_{i=1}^{2}\sum_{k=0}^{k_1} e(k)e(k-i)(\sum_{l=0}^{k} l_i e(l)e(l-i) + f'_i(-1) + q_i e(k)e(k-i) - a_i) \\
&+ \sum_{i=1}^{2}\sum_{k=0}^{k_1} e(k)\theta_F^m(k-i)(\sum_{l=0}^{k} \lambda_i e(l)\theta_F^m(l-i) + h'_i(-1) + \mu_i e(k)\theta_F^m(k-i) + \bar{a}_i - a_i) \\
&+ \sum_{i=0}^{1}\sum_{k=0}^{k_1} e(k)u(k-i-1)(\sum_{l=0}^{k} \rho_i e(l)u(l-i-1) + g'_i(-1) + \sigma_i e(k)u(k-i-1) - b_i)
\end{aligned} \tag{13}
$$

in which the second term in right side of Eq. (13) has

$$
\begin{aligned}
&\sum_{i=1}^{2}\sum_{k=0}^{k_1} e(k)\theta_F^m(k-i)(\sum_{l=0}^{k} \lambda_i e(l)\theta_F^m(l-i) + \mu_i e(k)\theta_F^m(k-i) + h'_i(-1) + \bar{a}_i - a_i) \\
&= \sum_{i=1}^{2}(\frac{\lambda_i}{2}(\sum_{k=0}^{k_1} e(k)\theta_F^m(k-i) + \frac{h'_i(-1)+\bar{a}_i-a_i}{\lambda_i})^2 + (\frac{\lambda_i}{2}+\mu_i)\sum_{k=0}^{k_1}(e(k)\theta_F^m(k-i))^2 - \frac{(h'_i(-1)+\bar{a}_i-a_i)^2}{2\lambda_i}) \\
&\geq -\sum_{i=1}^{2}\frac{(h'_i(-1)+\bar{a}_i-a_i)^2}{2\lambda_i} \\
&= -r_h^2
\end{aligned} \tag{14}
$$

in which $r_h^2 = \sum_{i=1}^{2} \frac{(h'_i(-1)+\bar{a}_i-a_i)^2}{2\lambda_i}$. Similarly we can obtain:

$$\sum_{i=1}^{2}\sum_{k=0}^{k_1} e(k)e(k-i)(\sum_{l=0}^{k} l_i e(l)e(l-i) + f'_i(-1) + q_i e(k)e(k-i) - a_i) \geq -r_f^2 \quad (15)$$

$$\sum_{i=0}^{1}\sum_{k=0}^{k_1} e(k)u(k-i-1)(\sum_{l=0}^{k} \rho_i e(l)u(l-i-1)+g'_i(-1) + \sigma_i e(k)u(k-i-1) - b_i) \geq -r_g^2 \quad (16)$$

in which, $r_f^2 = \sum_{i=1}^{2} \frac{(f'_i(-1)-a_i)^2}{2l_i}$, $r_g^2 = \sum_{i=0}^{1} \frac{(g'_i(-1)-a_i)^2}{2\rho_i}$.

By combining Eq. (13) with Eqs. (14-16) , we can have $\eta(0,k_1) = \sum_{k=0}^{k_1} w(k)v(k) \geq -r_0^2$, so that the nonlinear feedback link from $v(k)$ to $w(k)$ in Fig. 7 satisfies the Popov integral inequality. Q.E.D.

Remark: The calculation of $e(k)$ in Eq. (12) needs to use the values of the $f_i(k)$, $g_i(k)$ and $h_i(k)$ at the time k, which are not calculated out, so Eq. (12) can not be used to get $e(k)$ directly. We construct a forecast error $e^o(k)$ of $e(k)$ by using the parameters $f'_i(k-1)$, $g'_i(k-1)$ and $h'_i(k-1)$ at time $(k-1)$ to replace $f_i(k)$, $g_i(k)$, $h_i(k)$ in Eq. (12) :

$$e^o(k) = \sum_{i=1}^{2} \begin{bmatrix} a_i - f_i'(k-1) \\ a_i - \bar{a} - f_i'(k-1) \\ b_{i-1} - g'_{i-1}(k-1) \end{bmatrix}^T \begin{bmatrix} e(k-i) \\ \theta_F^m(k-i) \\ u(k-i) \end{bmatrix} \quad (17)$$

By Eq. (12) subtracting Eq. (17) and considering the relations between $f'_i(k-1)$, $g'_i(k-1)$, $h'_i(k-1)$ and the $e(k-1)$ in equation 10 at the time $(k-1)$, we can obtain the actual calculation formation of error $e(k)$ is shown in Eq. (11) .

3.2 Design of ASTKF

In order to eliminate the system disturbance and noise and improve the performance of the ATP system futher more, we'll apply an adaptive strong tracking Kalman filter to the system. An overview of the ASTKF is shown in Fig. 8 which is the Kalman filter in Fig. 5. A=$[0, -a_2; 1, -a_1]$ is the state transition matrix of $G(z)$, B=$[b_1; b_0]$ is the control matrix, Γ=$[b_1; b_0]$ is the state perturbation transition matrix, and C= [0,1] is the observation matrix, $x(k)$=$[\dot{\theta}_F(k); \theta_F(k)]$ is the system state at time k, representing the angular velocity and rotation angle of FSM; $x^*(k)$ is the predicted value of $x(k)$, $\hat{x}(k)$=$[\hat{\dot{\theta}}_F(k); \hat{\theta}_F(k)]$ is the estimated value of $x(k)$. $d_\theta(k)$ is the state disturbance and $v_\theta(k)$ is the measurement noise, $\theta'_F(k)$ is the output of the original controlled object system, representing the rotation angle of FSM, $\theta_F^*(k)$ is the predicted output of the constructed prediction system, $\tilde{\theta}_F(k)$= $\theta'_F(k) - \theta_F^*(k)$ is the output error between the original controlled object system and the constructed prediction system, $\hat{\theta}_F(k)$ is the estimated value of $\theta_F(k)$, representing the filtering output value $\theta_F^o(k)$, $\hat{q}(k)$ is the estimated value of the state disturbance. $\hat{Q}(k)$ is the estimated variance of the state disturbance. r is the mean value of measurement noise. R is the variance of measurement noise. $K_f(k)$ is the Kalman filter gain.

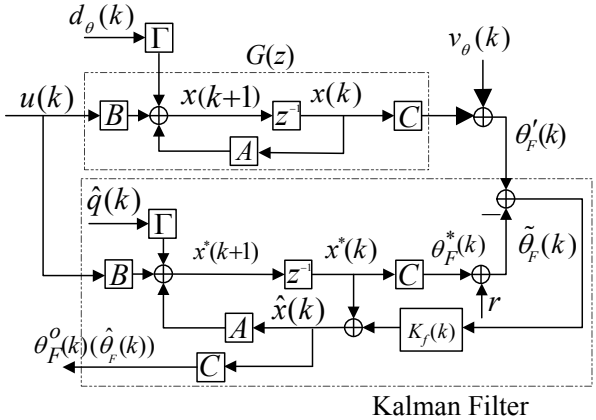

Figure 8: Structure of MRAC with Kalman Filter

The idea of ASTKF filter is that adaptive on-line iterative estimation is applied to estimate the mean

and variance of unknown state disturbances as $\hat{q}(k)$ and $\hat{Q}(k)$, respectively, and design the Kalman filter gain in combination with the state prediction variance $P^*(k)$.

$$K_f(k) = P^*(k)C^T[CP^*(k)C^T + R]^{-1} \tag{18}$$

The Kalman filter gain can correct the predicted value $x^*(k)$ of the state, and get the estimated value $\hat{x}(k)$. The strong filtering algorithm used in this paper adopts a fading factor $\lambda(k)$ when calculating the state prediction variance $P^*(k)$ based on the adaptive Kalman filtering algorithm, and combines the estimated variance $\hat{P}(k-1)$ of the previous moment to adjust the prediction variance of the state in real time $P^*(k) = \lambda(k)A\hat{P}(k-1)A^T + \Gamma\hat{Q}(k-1)\Gamma^T$; $\lambda(k)$ is a strong tracking fading factor and can be calculated as

$$\begin{aligned}
\lambda(k) &= \begin{cases} 1, & \lambda_0(k) < 1 \\ \lambda_0(k), & \lambda_0(k) \geq 1 \end{cases} \\
\lambda_0(k) &= \frac{tr(N_k)}{tr(M_k)} \\
N_k &= V(k) - C\Gamma Q(k-1)\Gamma^T C^T - lR(k) \\
V(k) &= \begin{cases} \tilde{\theta}_F(1)\tilde{\theta}_F(1)^T, & k = 1 \\ \dfrac{\rho V(k-1) + \tilde{\theta}_F(k)\tilde{\theta}_F(k)^T}{1+\rho}, & k \geq 2 \end{cases} \\
M_k &= CAP(k-1)A^T C^T
\end{aligned} \tag{19}$$

$\rho \in [0,1]$ is the forgetting factor in strong tracking system, $l \geq 1$ is as the weakening factor. $\hat{P}(k)$ is the state estimation covariance; $\hat{q}(k)$ is the estimated mean value of the state disturbance; $\hat{Q}(k)$ is the estimated variance of state disturbance; $\alpha(k-1)$ is the time variable estimation correction factor, $\tilde{\theta}_F(k)$ is the output error; $x^*(k)$ is the state predicted value, the expressions of the variables are shown in Eq. (20) .

$$\begin{aligned}
\hat{P}(k) =& [I - K_f(k)C]P^*(k) \\
\hat{q}(k) =& (1-\alpha(k-1))\hat{q}(k-1) + \\
& \alpha(k-1)\{(\Gamma^T\Gamma)^{-1}\Gamma^T \\
& [\hat{x}(k) - A\hat{x}(k-1) - Bu(k-1)]\} \\
\hat{Q}(k) =& (1-\alpha(k-1))\hat{Q}(k-1) + \\
& \alpha(k-1)\{(\Gamma^T\Gamma)^{-1}\Gamma^T \\
& [K_f(k)\tilde{\theta}_F(k)\tilde{\theta}_F(k)^T K_f(k)^T + \\
& \hat{P}(k) - A\hat{P}(k-1)A^T]\Gamma(\Gamma^T\Gamma)^{-1}\} \\
\alpha(k-1) =& \frac{1-c}{1-c^k} \\
\tilde{\theta}_F(k) =& \theta'_F(k) - Cx^*(k) - r \\
x^*(k) =& A\hat{x}(k-1) + Bu(k-1) + \Gamma\hat{q}(k-1)
\end{aligned} \tag{20}$$

The filtering output $\theta_F^o(k)$ can be formulated by

$$\theta_F^o(k) = \hat{\theta}_F(k) = C\hat{x}(k) \tag{21}$$

in which, $\hat{x}(k) = x^*(k) + K_f(k)\tilde{\theta}_F(k)$ and $x^*(k) = A\hat{x}(k-1) + Bu(k-1) + \Gamma\hat{q}(k-1)$, $K_f(k)$ can be calculated by Eq. (18)

4 Numerical experiments and results analyses

In order to verify the disturbance rejection and robustness performance of the method proposed in this paper, three numerical experiments are carried out under the Simulink platform, the first one is the performance comparisons of MRAC, ADRC and PID methods without using Filter in one axis, the second one is the performance comparisons of MRAC, ADRC and PID with ASTKF designed in one axis, the third one is the tracking control simulation experiments for of two axes with ASTKF.

4.1 Performance comparisons of MRAC, ADRC and PID methods without using Filter

In the experiment, the parameters in FSM are set as : $\omega = 9420$, $\eta = 0.7$, simulation period T=0.0004 s. Put these three values into Eq. (2) , we get the coefficients in the discrete transfer function of the FSM as

: $a_1 = 0.1288, a_2 = 0.005117,\ b_0 = 1.034, b_1 = 0.1$; Then the coefficients in the state space function in the controlled system are :

$$A = [0, -0.005117; 1, -0.1288]$$
$$B = [0.1, 1.034]$$
$$C = [0; 1]$$
$$D = 0$$

The reference model in the MRAC system are set as $\bar{a}_1 = 0.174$, $\bar{a}_2 = -0.051$, $\bar{b}_0 = 0.649$, $\bar{b}_1 = 0.228$, and $\lambda_1 = 0.1, \lambda_2 = 0.5, \mu_1 = 1, \mu_2 = 2, \rho_0 = 1.05, \rho_1 = 4, \sigma_0 = 1.5, \sigma_1 = 1.1, l_1 = 1, l_2 = 1, q_1 = 1.5, q_2 = 1.5$, the initial settings for each parameter in equation 10 are $h_1^{'}(-1) = 0, h_2^{'}(-1) = 0, g_0^{'}(-1) = 15.5, g_1^{'}(-1) = 1, f_1^{'}(-1) = 0.563, f_2^{'}(-1) = 0.217$. Furthermore, ADRC experiment is also designed and implemented referred in the paper [20], in which, the acceleration r_0=65000, the filter factor h_0=0.0032 in the transition process, the damping factor c=0.0188, the accuracy factor h_1=0.5384, the control gain r=450 in the nonlinear function fhan(e_1, e_2, c, r, h_1) of nonlinear controller [20](The nonlinear function is in Appendix 2), the compensation factor b_0=4.94 β_{01}= 1, β_{02}= 2.2822, β_{03}= 3.0591 in the extended state observer. PI controller parameters are : k_p =0.13, k_i =0.4.

The numerical experiments results are shown in Figs. 9-10, in which Fig. 9 is the angle error curves between output of the system and the desired input in the whole process of coarse and fine tracking, and Fig. 10 shows the fine tracking error. As can be seen from Fig. 9 that the PID, ADRC and MRAC can make the output quickly track the input signal. When the tracking error is less than 500 μrad, the time is at 0.796 s, the fine tracking system is starting to work. Tracking error can reach the steady-state tracking area at 0.892 s. One can see from Fig. 10 that the fine tracking error during steady-state tracking area after 0.892 s, and the tracking error by using MRAC can be as low as 2 μrad.

In order to further improve the tracking accuracy, ASTKF is added on the basis of the above three control schemes.

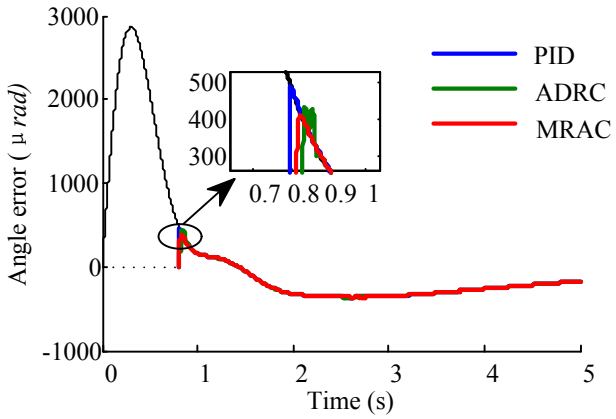

Figure 9: Angle errors of the coarse and fine tracking system.

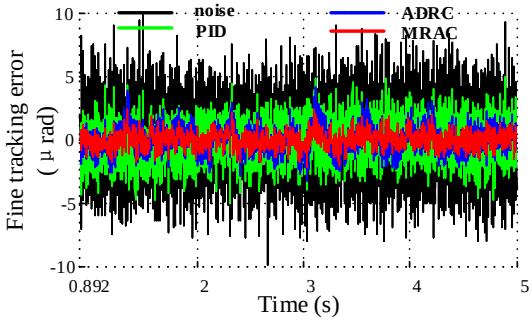

Figure 10: Comparative fine tracking errors of three methods.

4.2 Performance comparisons of MRAC, ADRC and PID with ASTKF

In this subsection, we perform the numerical experiments when adding the filter. Parameters of ASTKF are set as follows, c=0.47, $\hat{q}(0)$=0, $\hat{Q}(0)$=0, $\hat{x}(0)$=[0;0], $\hat{P}(0)$=[0.1, 0; 0, 0.1], R=6.115, l=20, ρ=0.9. The experimental results are shown in the Fig. 11, compared with Fig. 10, one can see that the tracking error of the three control strategies with ASTKF is significantly better than the tracking error without filter done in 4.1, and the tracking performance of the method with MRAC + ASTKF is the best, the tracking error can be reached within 1.5 μrad. To highlight the contrast, we calculate the probability that the tracking error fell within 2 μrad and the tracking error value with 99% probability. The experimental results are shown in TABLE 1. From TABLE 1 one can conclude that when adopting MRAC + ASTKF method, the fine tracking error less than 2 μrad with 99.84%

probability, which is biggest among all methods, and the corresponding fine tracking error can reach 1.3125 μrad, which is smallest.

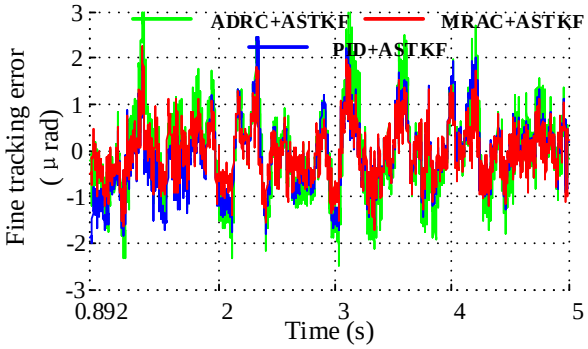

Figure 11: Comparative experimental results of three methods with filter

Table 1: Tracking errors and probabilities

Methods	Errors* (μrad)	Probabilities** (%)
MRAC+ASTKF	**1.3125**	**99.84**
ADRC+ASTKF	2.2951	96.56
PID+ASTKF	1.8101	99.70
MRAC	1.7618	99.63
ADRC	2.4637	96.14
PID	3.3746	86.72

* Tracking error with 99% probability
** Probabilities when tracking error is less than 2 μrad

4.3 Numerical experiments of two axes

From the analysis in subsection 4.1 and 4.2, MRAC with ASTKF is the best solution compared with PID and ADRC. Therefore, the numerical experiments of the two axes is carried out by MRAC with ASTKF, and the distribution of spots on the CMOS sensor is checked. This experiment considers both the x-axis and the y-axis of the fast reflector mirror (FSM). The parameters in the x-axis frame of FSM are set as $\omega = 9420, \eta = 0.7$, and for universality, the parameters in the y-axis are slightly different $\omega = 9000, \eta = 0.8$. At x-axis, the parameters in the reference model are $\bar{a}_1 = 0.174$, $\bar{a}_2 =$ -0.051, $\bar{b}_0 = 0.649$, $\bar{b}_1 = 0.228$, $\lambda_1 = 0.1, \lambda_2 = 0.5, \mu_1 = 1, \mu_2 = 2, \rho_0 = 1.05, \rho_1 = 4, \sigma_0 = 1.5, \sigma_1 = 1.1, l_1 = 1, l_2 = 1, q_1 = 1.5, q_2 = 1.5$, the initial settings for each parameter are $h_1^{'}(-1) = 0, h_2^{'}(-1) = 2.2, g_0^{'}(-1) = 15.5188, g_1^{'}(-1) = 1, f_1^{'}(-1) = 0.563, f_2^{'}(-1) = 0.2178$. The filter parameters are set as $c = 0.49$, $\hat{q}(0) = 0, \hat{Q}(0) = 0.1, \hat{x}(0) = [0; 0], \hat{P}(0) = [0.1, 0; 0, 0.1], R = 6.115, l = 20, \rho = 0.9$, and when at y-axis, only the forgetting factor c is changed to 0.47. Then the photons' distribution is shown in Fig. 12. One can see from Fig. 12 that when combining the functions of MRAC and ASTKF in fine tracking system, 99.7% of the photons can be projected into the square area within 2 μrad.

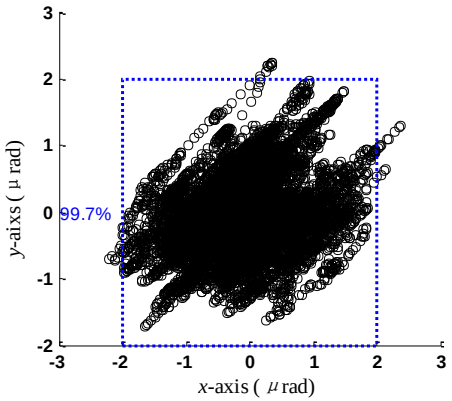

Figure 12: Photons' distribution

5 Conclusion

In this paper, the model reference adaptive control theory and adaptive strong tracking Kalman filter were applied to the fine tracking system. The mathematical model of each module based on the structure of the fine tracking system with the influence of state disturbance and measurement noise were established. The actual working environment of the fine tracking system was analyzed, and the continuous-angular vibration of the satellite platform was simulated with the SILEX satellite test data. A model reference adaptive control strategy and an adaptive strong tracking Kalman filter were designed to on-line estimate and eliminate the nonlinear disturbance and noise. The numerical experiments compared with ADRC, PID control were done. The comparison experimental results show that the MRAC strategy with ASTKF proposed in this paper has the best performance in the all compared methods and can achieve 2 μrad tracking error.

Appendix

Appendix 1. Deviation of acquisition of spot centroid and acquisition of angle

The angle tracking error calculation process is mainly divided into two steps: 1) acquisition of the spot centroid (x_c, y_c), 2) acquisition of the angle deviation $(\Delta\theta_F^x, \Delta\theta_F^y)$.

1) Acquisition of spot centroid

First, we define two coordinate systems: pixel plane coordinate system $x'Oy'$ and the detector three-dimensional coordinate system $Oxyz$. The coordinate origin O' of the coordinate system $x'Oy'$is at the center of the CMOS detector's surface, the coordinate x-axis and coordinate y-axis are established parallel to the two edges of the detector pixel, and axis unit length is a pixel size value d_a. Next, the coordinate origin O of the coordinate system $Oxyz$ is at the center of the CMOS detector lens's surface, and z-axis is along the direction of the origin O point to point O' in coordinate system $x'Oy'$, x-axis and y-axis are established in parallel to the sides of the detector cell by the right-hand theorem. Fig. 13 illustrates above two coordinate systems specifically. The coordinate transformation formula from a point (x', y') in coordinate systems $x'Oy'$ to (x, y, z) is

$$\begin{cases} x = d_a x' \\ y = d_a y' \\ z = f \end{cases} \tag{22}$$

in which, d_a is the size of the CMOS detector pixel, f is the focal length of the detector lens.

Generally, the spot centroid (x_c, y_c) is calculated by using the centroid algorithm, which is based on the principle of centroid in plane geometry. The spot centroid position is calculated as the pointing point of the beacon light on the detector. Define the spot's electrical energy signal which is distributed on the detector is: $\{v(x'y')|\,(x'y') \in S, S \in x'Oy'\}$, in which S is the surface area of the CMOS, so the centroid of the spot can be expressed as [21]

$$x_c = \frac{\sum\limits_{(x',y')\in S} x' \cdot W(x', y')}{\sum\limits_{(x',y')\in S} W(x', y')} y_c = \frac{\sum\limits_{(x',y')\in S} y' \cdot W(x', y')}{\sum\limits_{(x',y')\in S} W(x', y')} \tag{23}$$

in which

$$W(x', y') = \begin{cases} v(x', y') - v_{thresh}, v(x', y') \geq v_{thresh} \\ 0, \qquad\qquad\quad v(x', y') < v_{thresh} \end{cases} \tag{24}$$

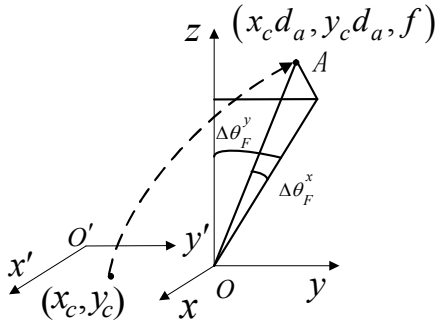

Figure 13: Coordinate transformation diagram

2) Acquisition of angle

The conversion relations of the angle deviation $\Delta\theta_F^x$ are shown in Fig. 13. Firstly, we convert the spot centroid (x_c, y_c) to the corresponding coordinate values at point A in the coordinate system $Oxyz$, in which on the yOz plane basis, the angle between the OA line and the yOz plane is the pitching angle $\Delta\theta_F^x$, and the angle between OA's projection line on the plane yOz and z axis is the azimuth $\Delta\theta_F^y$, thus $\Delta\theta_F^x$and $\Delta\theta_F^y$ can be obtained by the calculations of

$$\begin{cases} \Delta\theta_F^x = \arctan \dfrac{x_c d_a}{\sqrt{(y_c d_a)^2 + f^2}} \\ \Delta\theta_F^y = \arctan \dfrac{y_c d_a}{f} \end{cases} \tag{25}$$

For the reason that the unit of f is meter (m), which is far greater than the unit μm of d_a, equation 25 can be simplified as

$$\begin{cases} \Delta\theta_F^x = \arctan\dfrac{x_c d_a}{\sqrt{(y_c d_a)^2 + f^2}} \approx \dfrac{x_c d_a}{\sqrt{(y_c d_a)^2 + f^2}} \approx \dfrac{x_c d_a}{f} \\ \Delta\theta_F^y = \arctan\dfrac{y_c d_a}{f} \approx \dfrac{y_c d_a}{f} \end{cases} \tag{26}$$

Appendix 2. Nonlinear function "fhan" used in ADRC

fhan(e_1, e_2, c, r, h_1) is expressed as follows

$$\begin{cases} d = r \cdot h_1 \\ d_0 = h_1 \cdot d; \\ e_3 = e_1 + h_1 \cdot e_2; \\ a_0 = \sqrt{d^2 + 8r \cdot |e_3|} \\ \text{fhan} = -r \cdot \text{sat}(a, d); \end{cases} \tag{27}$$

where,

$$a = \begin{cases} e_2 + \dfrac{(a_0 - d)}{2}\text{sign}(e_3), |e_3| > d_0 \\ e_2 + \dfrac{e_1}{h_0}, \qquad\qquad |e_3| \le d_0 \end{cases}$$

and sat(a, d) is defined below

$$\text{sat}(a, d) = \begin{cases} \dfrac{a}{d}, & |a| \le d \\ \text{sign(a)}, & |a| > d \end{cases}$$

Acknowledgements: This work was supported by the National Natural Science Foundation of China under Grants 61973290 and Beijing Institute of Satellite Information Engineering, State Key Laboratory of Space-Ground Integrated Information Technology under Grants 2015_SGIIT_KFJJ_DH_04.

References:

[1] Giovannetti V., Lloyd S., Maccone L.: Quantum-enhanced positioning and clock synchronization, **412**(6845), 417 (2001)

[2] Liao S. K., Cai W. Q., Liu W. Y.: Satellite-to-ground quantum key distribution. Nature, **549**(7670), 43 (2017)

[3] Ren J. G., Xu P., Yong H. L.: Ground-to-satellite quantum teleportation. Nature, **549**(7670), 70 (2017)

[4] Yin J., Cao Y., Li Y.H.: Satellite-to-ground entanglement-based quantum key distribution. Physical review letters, **119**(20), 200501 (2017)

[5] Khalighi M. A., Khalighi M.: Survey on free space optical communication: A communication theory perspective. IEEE communications surveys & tutorials, **16**(2), 2231-2258 (2014)

[6] Nadeem F., Kvicera V., Awan M.S.: Weather effects on hybrid FSO/RF communication link. IEEE journal on selected areas in communications, **27**(9), 1687-1697 (2009)

[7] Davaslıoğlu K., Çağıral E., Koca M.: Free space optical ultra-wideband communications over atmospheric turbulence channels. Optics express, **18**(16), 16618-16627 (2010)

[8] Zhang M., Liang Y.: Compound tracking in ATP system for free space optical communication. Proceedings of Mechatronic Science, Electric Engineering and Computer (MEC),2011 International Conference, Jilin, China(2011)

[9] Fadhil H. A., Amphawan K. K., Shamsuddin H. A.: Optimization of free space optics parameters: An optimum solution for bad weather conditions. Optik-International Journal for Light and Electron Optics, **124**(19), 3969-3973 (2013)

[10] Osborne R. W., Zhang X., Willett P.: Effect of sensor pixel size on tracking. Signal and Data Processing of Small Targets, **17**(4), 71-6 (2013)

[11] Hassan M. F., Alrifai M. T., Soliman H. M.: Observer-based controller for constrained uncertain stochastic nonlinear discrete-time systems. International Journal of Robust and Nonlinear Control, **26**(10), 2090-2115 (2016)

[12] Cui N., Liu Y., Chen X.: Active disturbance rejection controller of fine tracking system for free space optical communication. Proceedings of International Symposium on Photoelectronic Detection and Imaging 2013: Laser Communication Technologies and Systems, **89** (6), 13 (2013)

[13] Alvi B. A., Asif M., Siddiqui F. A.: Fast steering mirror control using embedded self-learning fuzzy controller for free space optical communication. Wireless personal communications, **76**(3), 643-656 (2014)

[14] Muñoz-Benavent P., Gracia L., Solanes J. E.: Sliding mode control for robust and smooth reference tracking in robot visual servoing. International Journal of Robust and Nonlinear Control, **28**(5) 1728-1756 (2018)

[15] Zhao W., Ren X., Gao X.: Synchronization and tracking control for multi-motor driving servo systems with backlash and friction. International Journal of Robust and Nonlinear Control, **26**(13), 2745-2766 (2016)

[16] Yoon H., Bateman B. E., Agrawal B. N.: Laser beam jitter control using recursive-least-squares adaptive filters. Journal of Dynamic Systems, Measurement, and Control, **133**(4), 1001 (2011)

[17] Perez-Arancibia N. O., Gibson J. S., Tsao T. C.: Observer-based intensity-feedback control for laser beam pointing and tracking. IEEE Transactions on control systems technology, **20**(1), 31-47 (2012)

[18] Kadir N., Aziz A. I., Chowdhury S. J.: Performance improvement of the tracking system of a satellite laser communication. International Journal of Computer Applications, **26**(6), 19-25 (2011)

[19] Chen C. Y., Yang H. M., Tong S. F.: Real-time simulation of satellite-platform vibration of space optical communication. Journal of System Simulation, **19**(16), 3834-3837 (2007)

[20] Lin D., Wu Y. M., Zhu F.: Research on Precision Tracking on Fast Steering Mirror and Control Strategy. Proceedings of IOP Conference Series: Earth and Environmental Science, **114**(1), 2009 (2018)

[21] Fu C., Jiang L., Ren G.: Experiment system of fast steering mirror. Opto-Electronic Engineering, **21**(3), 1-8 (1994)